High-coercivity copper-rich Nd-Fe-B magnets by powder bed fusion using laser beam method

Olivier Tosoni, Elisa Borges Mendonça, Joni Reijonen, Atte Antikainen, Lukas Schäfer, Stefan Riegg

DOI: 10.1016/j.addma.2023.103426

High-coercivity copper-rich Nd-Fe-B magnets by powder bed fusion using laser beam method

Olivier Tosoni[1] (olivier.tosoni@cea.fr), Elisa Borges[1] (elisa.borges_mendonca@mines-paristech.fr), Joni Reijonen[2] (joni.reijonen@vtt.fi), Atte Antikainen[3] (Atte.Antikainen@vtt.fi), Lukas Schäfer[4] (lukas.schaefer@tu-darmstadt.de), Stefan Riegg[4] (rieggste@gmail.com), Oliver Gutfleisch[4] (oliver.gutfleisch@tu-darmstadt.de)

[1] *Univ Grenoble Alpes, CEA, LITEN, DTNM, F-38000 Grenoble, France*
[2]*VTT Technical Research Centre of Finland Ltd, Kemistintie 3, 02150, Espoo, Finland*
[3]*VTT Technical Research Centre of Finland Ltd, Visiokatu 4, 33720, Tampere, Finland*
[4]*Technische Universität Darmstadt, Material Science, Alarich Weiss Strasse 16, 64287 Darmstadt, Germany*

Corresponding author: Olivier Tosoni - CEA-LITEN - 17 rue des Martyrs - Bât E P 126 - 38054 Grenoble CEDEX 9 - FRANCE

Highlights

- 40-µm mean-sized Nd-Fe-B powders with tailored compositions were developed for PBF-LB
- 4 wt.% Dy alloy composition close to sintered with 1% Cu content yields highest coercivity
- Fine-grained equiaxed microstructure with almost no α-Fe can be obtained
- Annealed PBF-LB-built Nd-Fe-B samples reach B_r = 0.62 T and H_{cj} = 1790 kA.m^{-1}

Keywords

Additive Manufacturing, Powder Bed Fusion, Nd-Fe-B, Permanent Magnets, Coercivity

Abstract

Additive manufacturing (AM) is an attractive processing route to make efficient use of rare-earth elements (REE) in systems containing complex-shaped rare-earth (RE) based magnets. Powder bed fusion using laser beam (PBF-LB) is one of the most promising technologies to obtain fully dense AM parts and has seen significant recent research efforts. However, most works use commercial Nd-Fe-B powders with a composition more suited for binder based AM methods, which reduces the parameter window and does not allow property enhancement by the application of annealing cycles. In this work, a close-to-industrial process route was developed in order to produce a narrow-distributed 40-µm Nd-Fe-B powder, derived from strip casting, hydrogen decrepitation and milling, with a composition close to the usual sintered magnet grades having around 30 wt.% REE content. The composition was adjusted by preliminary small-scale experiments focused on the reduction of cracking and the promotion of fine-grained equiaxed microstructures. This powder was then used to build magnets by the PBF-LB method. The best magnetic properties could be achieved with building conditions providing just enough energy to completely melt the material, yielding nano-grained microstructures almost deprived of α-Fe phase. After laser parameter optimization and post-process annealing, properties of B_r = 0.62 T, H_{cj} = 1790 kA.m^{-1} and BH_{max} = 65 kJ.m^{-3} were obtained.

1. Introduction

Additive manufacturing (AM) of rare-earth (RE) permanent magnets (PM) is a relatively new research topic, aiming at enabling resource efficient production of RE-PM's with complex geometry and specific stray field distribution. RE-PM's and in particular Nd-Fe-B magnets play an important role in the energy transition and electrification of mobility, their demand will grow dramatically in the next decades [1]. Due to the concentration of the RE industry in a limited number of countries and with the growing demand driven by magnet applications required to combat climate change, the markets are prone to supply shortages, sharp price fluctuations and unwanted geopolitical dependencies, which are detrimental for the industry and more generally, the transition to a net-zero CO_2 emission scenario. Besides the search for materials containing less RE and the enhancement of extrinsic properties of the existing hard magnetic materials [2] [3], net-shape processes like powder injection molding or additive manufacturing appear as a way to use magnets more efficiently without wasting material in the machining step to final geometry.

AM is by nature a near-net-shape manufacturing process generating minimal waste, and it enables much higher geometrical freedom than conventional magnet manufacturing processes of pressing and sintering or injection molding, which enable the design and manufacture of optimized magnetic topologies. However, research on AM of functional materials such as Nd-Fe-B, which has a very specific microstructure and tailored grain boundaries required to transfer the intrinsic magnetic properties of the alloy into the bulk magnet, has been only initiated in the past couple of years, as the focus of AM materials research has been previously on structural materials.

The most straightforward way to additively manufacture Nd-Fe-B magnets, which has been applied by several authors, is to use a polymer-based AM method with commercially available coercive Nd-Fe-B powder mixed with PA12 as binder to make bonded magnets [4] [5]. Other authors propose a method to form an epoxy-based ink with the Nd-Fe-B powder [6]. Due to the absence of grain alignment (texture), the magnetic properties remained low (remanence below 0.45 T).

Gandha *et al.* [7] used material extrusion based big area additive manufacturing (BAAM) to produce anisotropic bonded Nd-Fe-B magnets (70 vol.% MQA-38-14 Nd-Fe-B powder, 30 vol.% nylon-12) with properties of H_{cj} = 1030 kA.m^{-1}, B_r = 0.94 T and BH_{max} = 140 kJ.m^{-3}. Grain alignment was induced by applying a post-process heat treatment in a magnetic field at temperatures high enough to soften the nylon-12 matrix and allow for the Nd-Fe-B particles to align with the field. The same group then proposed a mathematical analysis using a multiphysic modelling of the alignment process in a powder/polymer mixture under magnetic field in order to help predict the magnetic properties in a functionalized AM machine [8]. Although the magnetic properties are promising as they are comparable to injected anisotropic bonded magnets [9], the major downside of this approach is the poor dimensional accuracy and surface finish to the finished magnets.

To get the maximum properties from Nd-Fe-B magnets, it is desirable to manufacture fully dense and textured magnets (such as sintered magnets are) without any binder (such as polymer bonded magnets). From all available AM technologies, powder bed fusion using laser beam (PBF-LB) is best suited for producing fully dense metallic parts with high geometrical freedom, good dimensional accuracy and reasonable surface finish [10] [11]. Furthermore, the highly selective and localized laser melting in the PBF-LB process enables the formation of fine-grained microstructures and is well suited for processing alloys where rapid solidification is of benefit [12], as with Nd-Fe-B. It must be noted that post process heat treatments are often required after PBF-LB to reach optimal microstructure and properties [13].

An early work on the PBF-LB of RE-transition metal compounds is the one from Moore *et al.* in 2013 where magnetocaloric heat exchangers with specific internal porosity or microchannels were produced from $La(Fe,Si)_{13}$ [14].

Jacimovic *et al.* [15] were first to report fully dense (with no binder matrix) Nd-Fe-B magnets processed by PBF-LB. They used a commercially available gas atomized nanocrystalline RE-lean Nd(Pr-Zr-Ti-Co)-Fe-B MQP-S-11-9 spherical powder from Magnequench and claimed properties of H_{cj} = 695 kA.m^{-1}, B_r = 0.59 T, and BH_{max} = 45 kJ.m^{-3} in the as-built magnets. According to the authors, the rapid solidification during the process enabled the re-formation of a nanocrystalline microstructure similar to the one of the starting powder, and the realization of hard magnetic properties. Several other groups addressed the synthesis of Nd-Fe-B magnets by PBF-LB [16] [17] [18]. Among them, Bittner *et al.* [19] [20] optimized the laser melting parameters to enhance the properties of this alloy further to H_{cj} = 921 kA.m^{-1}, B_r = 0.63 T and BH_{max} = 63 kJ.m^{-3}. Huber *et al.* [21] used grain boundary infiltration with low melting point eutectic alloys to further enhance the coercivity of PBF-LB processed MQP-S powder to 1211 kA.m^{-1} when infiltrated with $Nd_{50}Tb_{20}Cu_{30}$. The disadvantage of this method is the additional processing step and the corresponding decrease in volume fraction of the 2-14-1 phase and hence remanence (0.39 T in their case). Volegov *et al.* [22] used a powder mixture of 80% MQP-B powder with 20% $(NdPr)_3Cu_{0.25}Co_{0.75}$ powder to realize in-situ and in one single step the infiltration during the building of the parts, and obtained an even higher room-temperature coercivity of about 1250 kA.m^{-1}.

Goll *et al.* [13] took the RE-lean MQP-S-11-9 composition used by multiple research groups and added excess RE to synthesize stoichiometric and over-stoichiometric powder compositions to be manufactured with PBF-LB. With 18 at.% RE and 2-step post-process annealing (600°C for 10 min, then 500°C for 60 min), properties of H_{cj} = 925 kA.m^{-1}, B_r = 0.58 T, BH_{max} = 62.3 kJ.m^{-3} were achieved. Laser parameters leading to extremely rapid solidification during PBF-LB, combined with post-process annealing was found to be important in realizing high coercivity microstructure (formation and wetting of the RE-rich grain boundary phase).

An alternative approach by using RE-rich Pr-Fe-Cu-B material for PBF-LB was investigated by Schäfer *et al.* [23]. The authors show that subsequent heat treatments can significantly increase the coercivity, which is accompanied by the formation of an intermetallic $Pr_6Fe_{13}Cu$ secondary phase. Goll *et al.* [24] further demonstrated the possibility to produce a textured microstructure in such $Fe_{73.8}$-$Pr_{20.5}$-$Cu_{2.0}$-$B_{3.7}$ alloy magnets by using a non-rotating laser scanning strategy. This resulted in notable grain alignment along the laser scanning direction and increase from 0.5 T (isotropic structure) to 0.67 T in remanence.

In this work, a Cu-rich Nd-Fe-B alloy and powder were developed, with a composition otherwise close to Dy-doped sintered magnets for PBF-LB processing. This work was carried out in the framework of the EIT Raw Materials funded KIC project 3DREMAG, whose main objective was the development, upscaling and demonstration of an alternative Nd-Fe-B powder for AM. Therefore, all the processing steps for the production of the powder have been voluntarily kept as close as possible to the established production routes of Nd-Fe-B magnets and a demonstration of scalability was realized (pre-industrial 63-kg batch of powder). After laser parameter optimization and post-process annealing, properties of B_r = 0.62 T, H_{cj} = 1790 kA.m^{-1} and BH_{max} = 65 kJ.m^{-3} were obtained. This represents the highest ever reported coercivity for additively manufactured Nd-Fe-B; remanence and energy product remain in the range of other PBF-LB reports and lower than reports with additive manufacturing processes allowing grain alignment.

2. Materials and methods

2.1 Methodology

For this work, three experimental steps, which are in short single track scanning, suction casting, and the AM of simple shaped magnets, have been used to obtain additively manufactured magnets with hard magnetic properties.

The single track scanning (laser melting along one track) was carried out on strip cast flakes fixed to the building platform. Different chemical compositions typical for sintered Nd-Fe-B magnets have been used to compare the influence of stoichiometry on the melt pool geometry. This method has been used in various studies to study the laser-material interaction in the context of PBF-LB alloy research [25] [26] [27] [28] [29]. It allows to study the relationship between the most influencing laser melting parameters (speed and power) and the alloy composition in terms of melt pool size/shape, solidification microstructure and defect formation such as cracking in the case of brittle materials like Nd-Fe-B before the production of powder batches. This reduces the lead-time of alloy development for PBF-LB considerably during the first iterations with the given alloy.

The second step is suction casting experiments to simply test the composition of the alloy in laboratory scale. The suction casting process is used to test compositional modifications of strip cast alloys and the impact on their magnetic properties after rapid solidification. The cooling rate is estimated to reach orders of 10^3 $K.s^{-1}$ based on previous works [30] [31] [32]. Although it is not possible to simulate the local, complex melting and solidification behavior during PBF-LB, the suction casting is able to indicate trends based on the influence of compositional variations on the intrinsic magnetic rapidly solidified microstructure and the resulting extrinsic magnetic properties (coercivity and remanence). Additional heat treatments can be easily applied to simulate the post process heat treatment for the AM parts.

These preliminary experiments allowed to identify an Nd-Fe-B alloy composition suitable to the PBF-LB process by performing dedicated small-scale experiments. The last step was therefore the larger scale (several kg) production of powder with this composition to additively manufacture parts with varying parameters to optimize the building conditions and understand the relationships between microstructure and macroscopic properties.

2.2 Experimental

Single-track scanning was conducted on 200-300 µm thick strip cast flake substrates having different chemical compositions typical for sintered Nd-Fe-B magnets. The six compositions that were used are summarized in the Table 1. Especially the varying proportion of the REE Nd and Dy as well as the total fraction of the REE and the boron level in the composition are known to strongly influence the magnetic properties. The flakes were mounted on the building plate as shown in Figure 1a. Their surfaces were wiped with Ethanol before processing to remove any dirt and grease. The laser melting experiments were performed using an SLM 125 HL PBF-LB system from SLM Solutions GmbH, having a IPG-YLR-400-SM fiber laser producing 400 W maximum nominal output power at 1070 nm wavelength. The x-y scanning on the processing plane is performed with a galvanometer scanner (intelliSCAN 25 from SCANLAB GmbH). After all the optics, the laser spot size is 80 ± 6 µm at focal plane with a Gaussian intensity distribution. Argon 5.0 was used as the shielding gas in the processing chamber, the atmosphere having oxygen content of < 0.1% during laser melting. Before the actual single tracks (as indicated with lines in Figure 1a), a square area of 10 x 10 mm^2 was laser-melted to have a more representative substrate microstructure to the actual situation of PBF-LB, where the previous laser-melted layer acts as the substrate. This has been shown to affect the single track studies [33]. 21 single tracks (6 mm length with 0.5 mm spacing) for the actual analysis were laser melted on each substrate, perpendicular to the scanning of the previously laser-melted surface. The

laser power was varied between 50 and 200 W and scanning speed between 500 and 2000 mm.s^{-1} in the single scan tracks. The test setup of the building platform is shown in Figure 1a for three mounted strip cast flakes.

Ref.	Dy	Nd	Pr	Al	B	Co	Cu	Ga	Ti	Zr	Fe	Total REE
Alloy A	0.51	23.3	7.38	0.19	1.04	0.94	0.10	0.16	0.05	0.02	Bal.	31.18
Alloy B	3.03	21.4	6.53	0.19	1.07	1.04	0.18	0.15	0.10	0.03	Bal.	30.95
Alloy C	-	25.4	7.97	0.28	0.95	0.53	0.14	0.11	0.05	0.00	Bal.	33.37
Alloy D	-	22.8	7.5	0.23	0.89	1.99	0.16	0.22	-	-	Bal.	30.30
Alloy E	3.7	21.7	6.1	0.12	1.03	1.10	0.11	0.20	-	-	Bal.	31.50
Alloy F	10.1	15.1	5.0	<0.02	0.96	1.98	0.17	0.21	-	-	Bal.	30.20

Table 1*: Chemical compositions (wt.%) of the studied strip cast flakes.*

After laser melting, the flakes were cross-sectioned perpendicular to the melt tracks, mirror polished and etched with Nital to reveal the melt pool boundaries and microstructure. Optical microscope images of the melt pool cross-sections were acquired using ZEISS Axio Observer Inverted Microscope at a magnification of 50x. The *ImageJ* software was used to measure the melt pool dimensions from the images. After that, around 0.5-1.0 mm of the material was ground, polished, etched and imaged again following the same procedure to have two cross-sections of each melt track analyzed for the presence of cracks. It is however acknowledged that this is not an absolute analysis of crack presence and some cracks that do not continue along the melt track for a considerable distance will remain unnoticed.

The suction casting experiments have been performed in a Buehler MAM-1 Arc Melter. The sample chamber was purged and flushed with Argon several times to prevent strong oxidation of the sample material. In the Cu cooling plate, a Cu mold is inserted with a 4 mm times 0.5 mm wide cavity. Attached to the Cu mold is a secondary vacuum chamber which induces the suction of the liquid metal into the Cu mold; the depth of the cavity is several centimeters, allowing all the material to be solidified before it reaches the opposite edge. The obtained suction cast plates were annealed at 1075°C for 30 minutes, then at 750°C for 1 h and finally at 500°C for 1 h, with a cooling speed of 300°C.h^{-1} between the plateaus. The temperatures and holding times for the heat treatment follows typical post processing treatment of Nd-Fe-B permanent magnets produced by powder metallurgical routes.

To prepare PBF-LB experiments, an 18 kg batch of alloy with the nominal composition $Nd_{12.1}Pr_{0.8}Dy_{1.5}Fe_{bal.}B_{6.3}Co_{1.24}Al_1Cu_1Ga_{0.2}$ was cast using a strip casting setup from ULVAC. The molten materials were induction heated up to 1450°C, then poured through two tundishes on a cooled rotating copper wheel having a linear speed 1.2 m.s^{-1}, to obtain ribbons with a 300 µm mean thickness. The ribbons were then submitted to a heat treatment at 1050°C under vacuum for 2 hours to grow the grains prior to hydrogen decrepitation (HD), and jet milling. This additional step allows avoiding the generation of excessively large amounts of fine particles due to the typical Nd-rich spacing of Nd-Fe-B strip cast ribbons being by one order of magnitude smaller than the targeted granulometry for AM; fine particles are known to decrease the flowability and spreadability of powders on the building platform. Hydrogen decrepitation was performed under 800 mbar H_2 pressure at 250°C: these conditions allow to reduce the amount of absorbed hydrogen compared to standard hydrogenation conditions (a few bar at room temperature) in order to adapt to the coarser granulometry needed for PBF-LB compared to sintering (medium size around 40 µm vs. 5 µm). Partial

dehydrogenation was obtained by exposing the decrepitated material to 550°C under primary vacuum for 3 hours. Jet milling was performed with a 3-nozzle opposed fluidized bed AFG100 setup from Hosokawa using a 3.5 bar N_2 pressure and 2.5 mm diameter nozzles. The granulometric parameters of the obtained 17 kg powder batch, measured through an in-line analysis with a laser diffraction granulometer from Malvern Analytics, are the following: d_{10} = 18 µm, d_{50} = 42 µm and d_{90} = 85 µm. A micrography of the powder and its granulometric distribution are shown in Figure 2, confirming the very low amount of fine particles (below 10 µm). Eventually, the powder was sieved (mesh = 50 µm) in order to remove bigger particles before being used for PBF-LB experiments, with a yield above 99%. This yield is higher than one would expect according to the granulometry of the powder, which is explained by the observed irregularity in the particles' shapes.

Finally, 10 mm diameter and 5 mm high cylindrical samples were produced by laser powder bed fusion under inert atmosphere (Ar 5.0, O_2 content in the building chamber below 1000 ppm) using a ProX200 AM machine from 3DSystems. The arrangement of the AM cylindrical samples on the building platform is shown in Figure 1b. The laser wavelength was λ = 1064 nm, the spot size was equal to 70 µm; laser power, laser speed and hatching distance were varied. The scanning pattern consisted of parallel lines, scanned in only one direction (no power during the return), with a rotation of 90° between two successive layers. Stainless steel substrates were used without any pre-heating. A few experiments were conducted with cubic instead of cylindrical samples, and some of them without rotation of the scanning lines between successive layers.

The non-spherical powder has a relatively poor spreading behavior compared to commercial spherical powders for other alloys, but the narrow granulometry and especially the low proportion of fine particles much below 10 µm allowed to process it in an equipment where the powder is not conveyed through narrow nozzles that might get clogged. Still, the spreading was improved thanks to surface preparation (roughening) of the substrate, allowing to increase the adherence of the powder to the substrate and avoid depletion. After the construction, parts were removed from the substrate by a sharp knock at the base, and their circular faces were manually rectified by polishing to make them parallel, yielding pieces of roughly 4 mm height for magnetic characterization. Annealing of the AM magnets was performed under secondary vacuum at temperatures between 400°C and 700°C, with a cooling rate of 30°C.min^{-1} after each plateau, here again following typical post processing treatment of Nd-Fe-B permanent magnets produced by powder metallurgical routes.

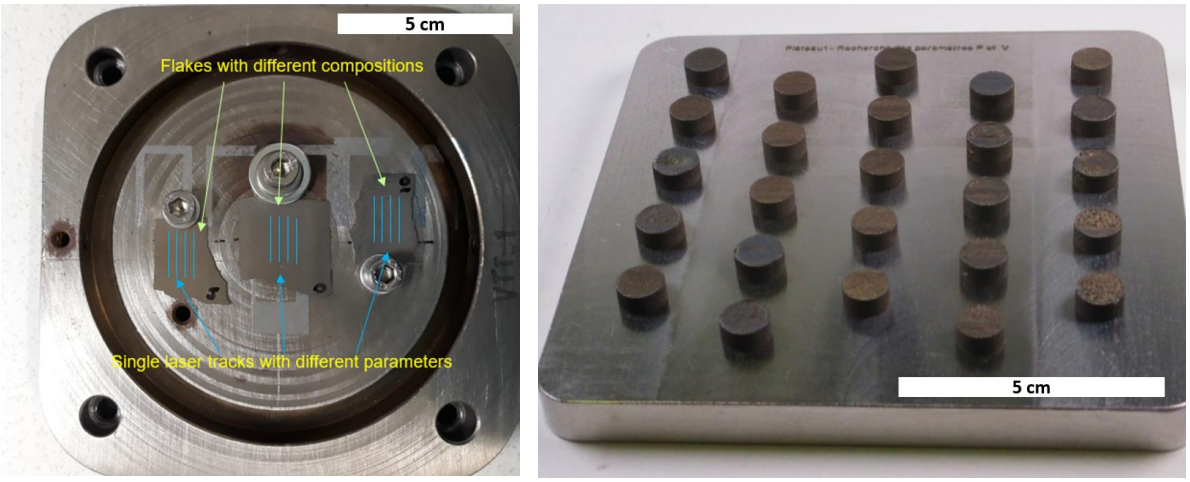

(a) **(b)**

Figure 1*: Views of the experimental building platform setup. (a) SLM 125 setup used for single laser track experiments on three flakes with marked examples for the tracks. (b) ProX200 setup for the AM of cylindrical parts with the powder of the selected alloy.*

Density measurements were performed with the Archimedes method in pure ethanol on as-build and polished samples. J-H curves were obtained with an AMH-300-P hysteresisgraph from Laboratorio Elettrofisico. Scanning Electron Microscopy (SEM) was carried out with a XL30 tungsten filament microscope from Philips and a MERLIN Field Emission Gun (FEG) microscope from Zeiss, both equipped with a back-scattered electron (BSE) detector for chemical contrast. Prior to microstructural characterization, samples were embedded in an epoxy resin and their surface was mirror polished with a diamond solution down to 1 µm roughness. The measurement of the oxygen content was performed by the Instrumental Gas Analysis method with a commercial equipment (EMGA-830 by Horiba).

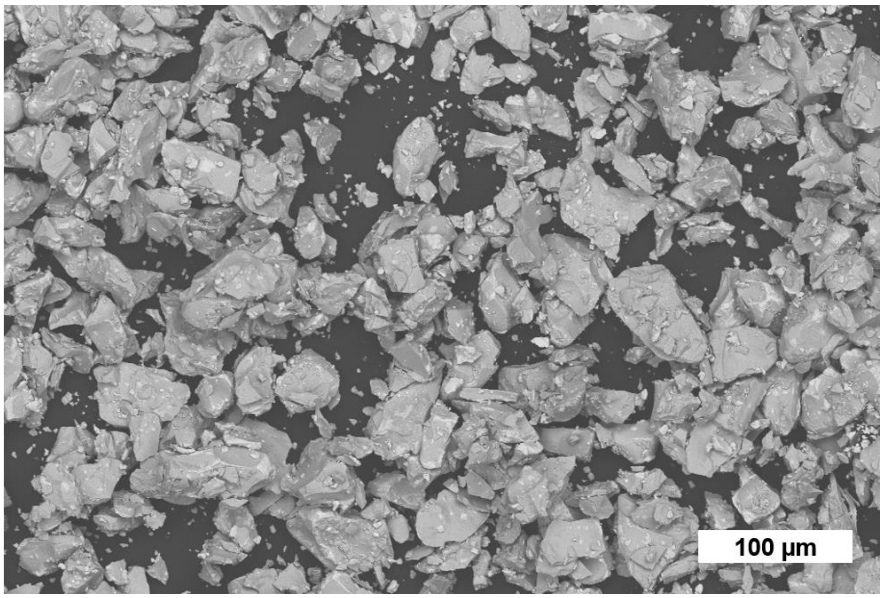

(a)

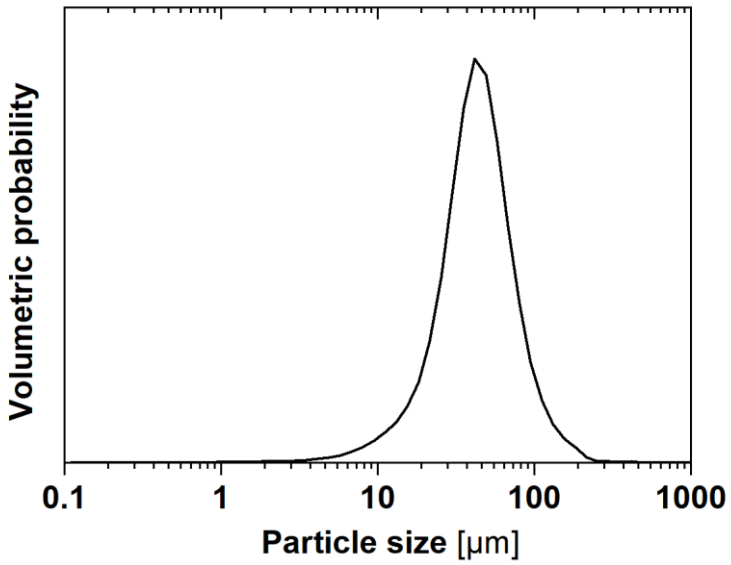

(b)

Figure 2*: (a) SEM picture of the Nd-Fe-B powder produced in this work and used for PBF-LB experiments in the ProX200 machine; (b) Volumetric particle size distribution of this powder, with* d_{10} *= 18 µm,* d_{50} *= 42 µm, and* d_{90} *= 85 µm.*

3. Results and discussion

3.1 Screening of alloys by single track melting experiments

The single track screening parameters were chosen based on prior experience of suitable energy density limits in PBF-LB of Nd-Fe-B. Figure 3a shows the cracks observed for all the studied laser parameter and alloy combinations and Figure 3b the number of cracks versus the RE content of the alloy. We have further marked in Figure 3a whether the cracking was observed in the heat-affected zone (**HAZ**), in the weld (**WELD**) or whether cracks were seen on both (**BOTH**), or if no cracks were detected (**-**). It can be seen that both type of cracks were observed in most of the alloys. As already reported [18] [34], cracking is always present to some extent, and increases with the energy density. The only alloy composition where cracks in the weld metal were not observed with any of the studied parameter combinations (which, as explained in the previous section, does not mean there was no cracking at all) was the Alloy E. It can be further seen that this alloy composition has the most parameter combinations that do not result in cracking in the heat-affected zone either (i.e. this alloy has the widest processing window).

Figure 4 shows the etched cross-sections of two single tracks on the Alloy E composition, produced with high (Figure 4a, 0.15 $J.mm^{-1}$) and low (Figure 4b, 0.06 $J.mm^{-1}$) linear energy input, resulting in significantly different melt pool sizes. With high energy input (Figure 4a), large melt pool is formed, with a relatively slow cooling rate resulting in mainly dendritic solidification microstructure. Dendrites as long as 65 µm grow from the edges towards the center of the melt pool. 89% of the total melt pool area as measured from the cross-section has a dendritic structure, the remaining being equiaxed in the center. With low energy input (and hence small melt pool, Figure 4b), only a small region (11% of total melt area) at the edges of the melt pool solidifies dendritically (5-6 µm long) as seen in Figure 4b, while the majority of the melt pool solidifies in an equiaxed grain structure due to extremely rapid cooling rate. It can be also seen that the Alloy E composition has a distinctively different behavior from the other studied compositions, namely that the effect of the laser parameters on the formation of dendritic or equiaxed structure is most pronounced.

Figure 5a shows the melt pool penetration depth and Figure 5b the width of the molten track as measured from the etched cross-sections for all the studied compositions as a function of laser line energy. Here again, it can be seen that the Alloy E composition distinguishes from the other ones by having the largest melt pools, which is related to thermal conductivity but can also be affected by the metastable melting point of the material [29]. This may explain the larger share of dendrites observed in the melt pools compared to the other compositions, as a larger melt pool would result in slower solidification rate and hence dendrite growth is promoted.

As stated before, the aim of this screening is not an optimization of the mechanical properties of the magnets, nor the complete suppression of cracks, but a comparative evaluation of the behavior of different Nd-Fe-B alloys in order to identify alloys that should be more prone to processing by PBF-LB. Cracking needs to be minimized but a stronger emphasis is made on magnetic properties in this work, provided that samples are mechanically stable enough for magnetic measurements. At this stage, Alloy E distinguishes from the others and seems a good candidate.

Speed [mm.s^{-1}]	Power [W]	Line energy [J.mm^{-1}]	Alloy A	Alloy B	Alloy C	Alloy D	Alloy E	Alloy F
1250	75	0.06	MELT	BOTH	BOTH	BOTH	-	MELT
1500	100	0.07	MELT	HAZ	HAZ	-	-	BOTH
1750	125	0.07	HAZ	HAZ	BOTH	MELT	HAZ	HAZ
2000	150	0.08	BOTH	BOTH	HAZ	-	-	BOTH
800	70	0.09	HAZ	MELT	-	-	-	HAZ
2000	200	0.10	HAZ	MELT	-	BOTH	-	HAZ
500	50	0.10	HAZ	HAZ	-	HAZ	-	HAZ
1500	150	0.10	HAZ	HAZ	HAZ	HAZ	HAZ	MELT
1000	100	0.10	HAZ	HAZ	HAZ	HAZ	-	HAZ
1750	175	0.10	BOTH	HAZ	-	HAZ	-	HAZ
1250	125	0.10	HAZ	BOTH	-	HAZ	-	HAZ
1300	160	0.12	HAZ	HAZ	HAZ	HAZ	-	MELT
1500	200	0.13	HAZ	HAZ	-	HAZ	-	-
1054	158	0.15	HAZ	-	HAZ	HAZ	-	BOTH
777	116.5	0.15	HAZ	HAZ	-	HAZ	-	HAZ
500	75	0.15	-	-	-	HAZ	-	HAZ
1250	200	0.16	-	HAZ	-	BOTH	N/A	BOTH
800	150	0.19	HAZ	HAZ	-	HAZ	HAZ	HAZ
1000	200	0.20	HAZ	HAZ	HAZ	HAZ	HAZ	HAZ

(a)

Figure 3: *Cracking tendency for the studied alloy compositions (a) as a function of the laser parameters:* **-** *corresponds to no cracks,* **HAZ** *to the presence of cracks in the heat-affected zone only;* **MELT** *in the melt pool zone; and* **BOTH** *in both zones; N/A corresponds to one isolated case where the laser vector missed the sample, so that no crack data was available.*

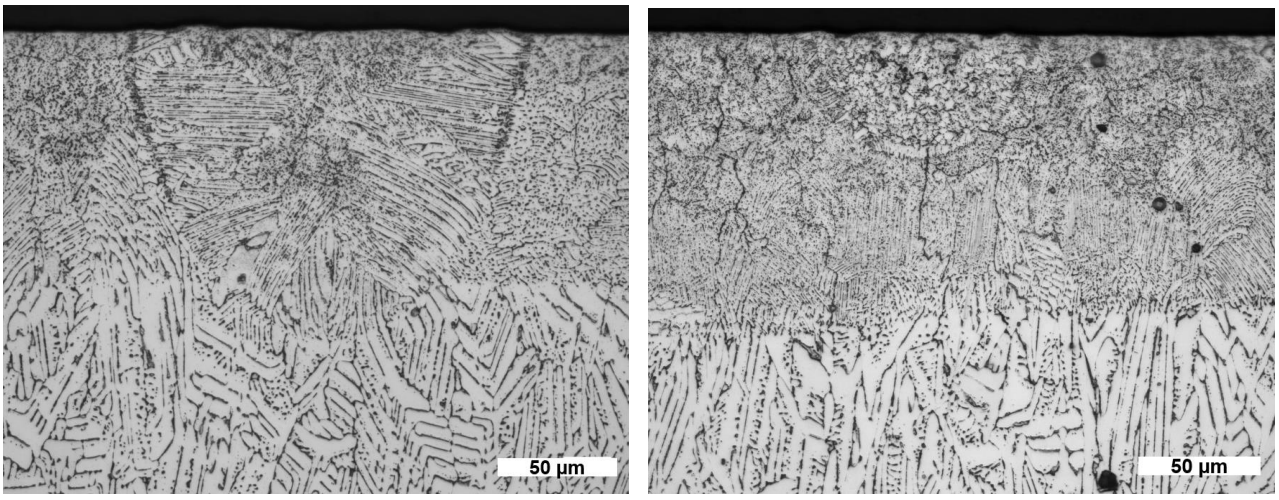

(a) (b)

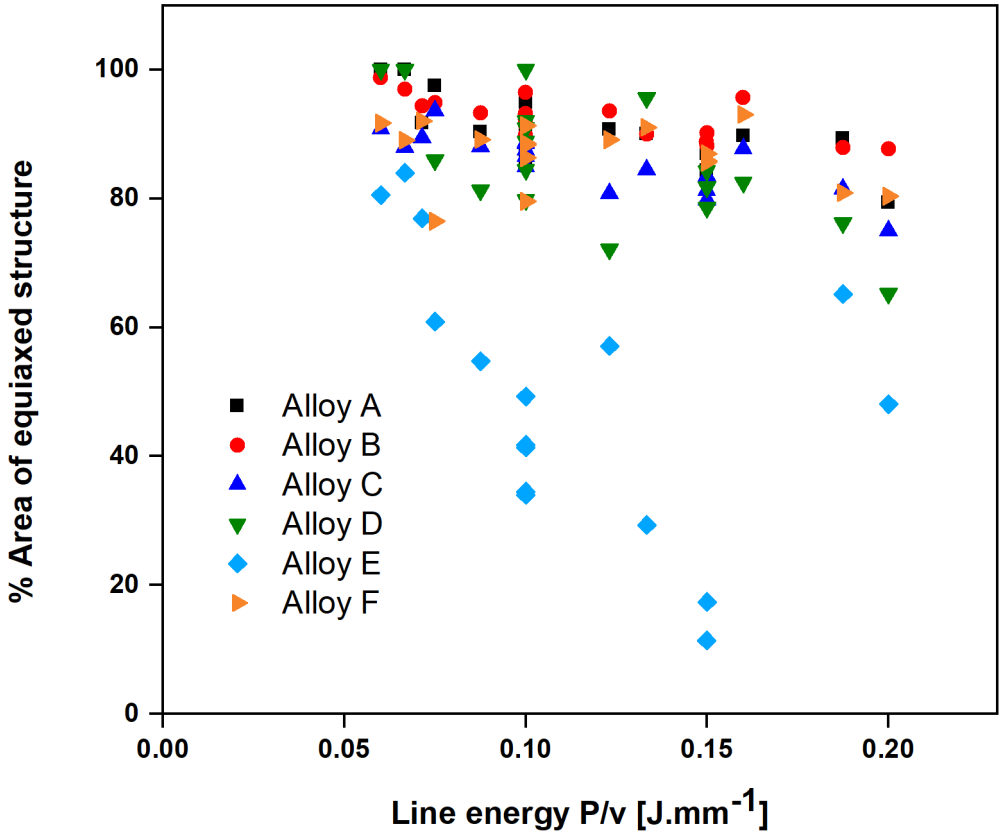

(c)

Figure 4*: Microstructures of solidified laser tracks in the Alloy E (a) dominantly dendritic (v = 1054 mm.s^{-1} / P = 158 W) and (b) (mainly equiaxed (v = 1250 mm.s^{-1} / P_{laser} = 75 W). Graph (c) shows the amount of equiaxed microstructure versus line energy in melt pool cross-sections in each alloy A-F. Notice the difference between the pre-laser melted substrate and the underlying strip cast microstructure, which was done to represent PBF-LB conditions more accurately.*

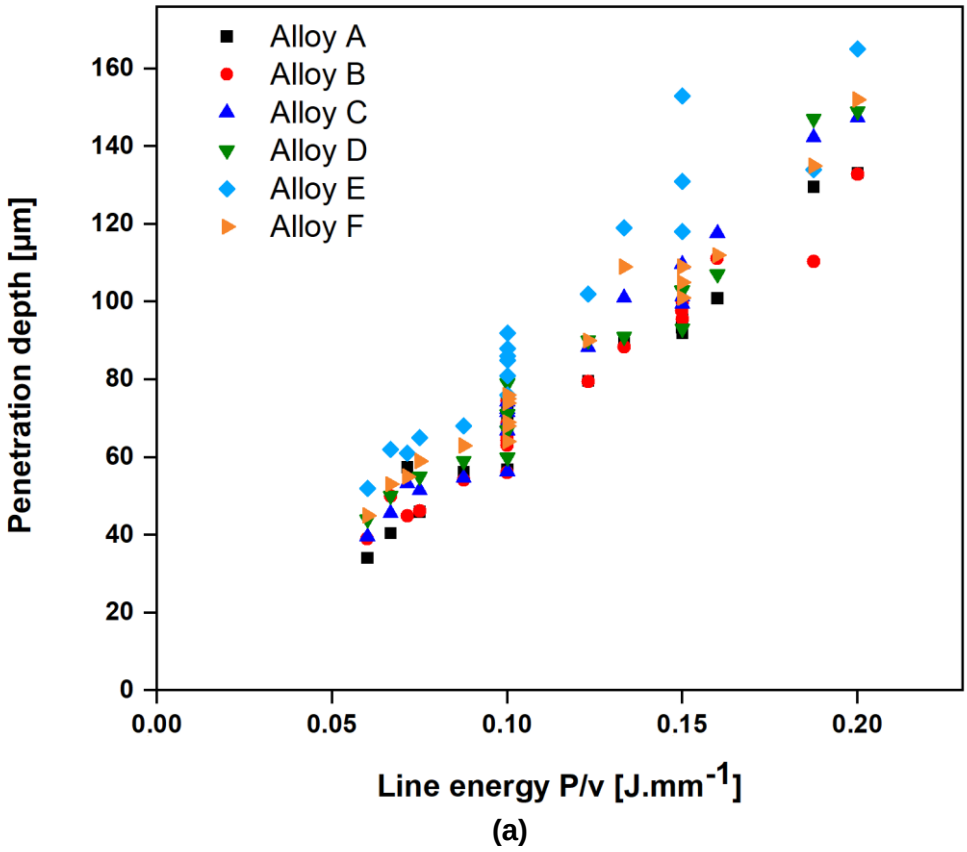

(a)

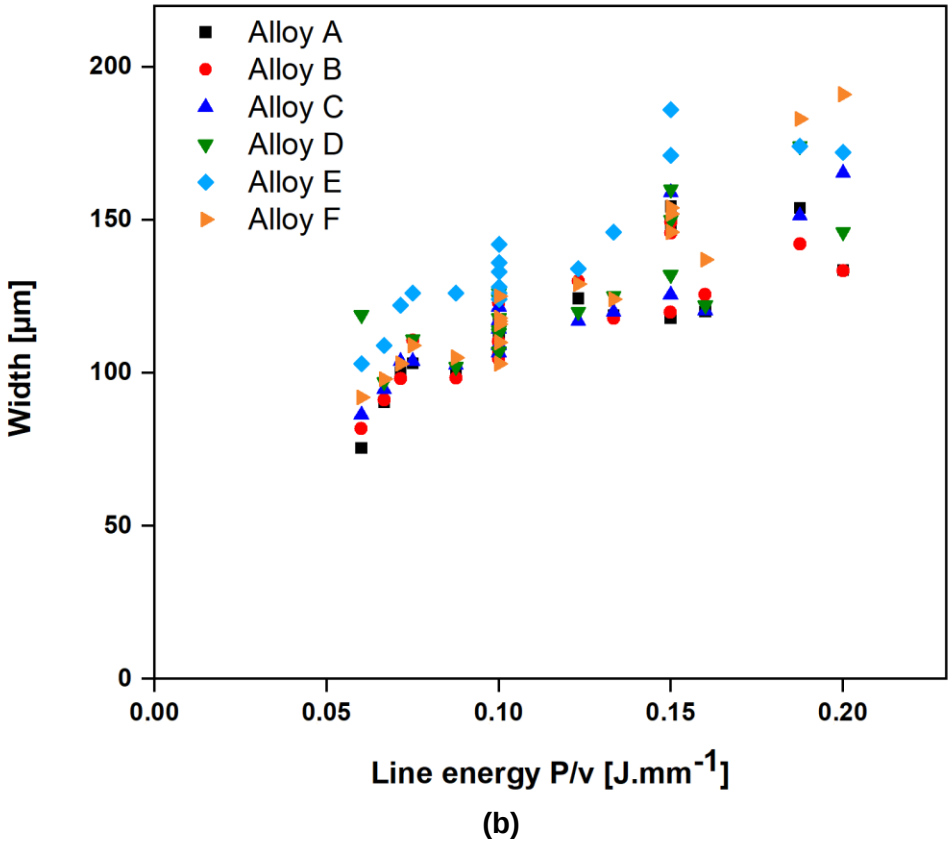

(b)

Figure 5*: Size of the melt pools measured from the cross-sections (a) penetration depth (b) width of the melt pool. Original data is provided in the Supplementary Material section (Table 3)*

3.2 Confirmation of the composition choice and investigation of the copper addition by suction casting

Three of the aforementioned alloys have been tested by suction casting, namely the alloys D, E, F, which differ mainly by their dysprosium content: no Dy for the Alloy D, 3.7 wt.% in the alloy E, and 10.1 wt.% in the Alloy F. The suction casting reproduces a form of rapid solidification whereby cooling rates of 10^3 K.s^{-1} can be achieved [30] [31] [32]. Although this technique cannot replace the optimization process and the local, complex melting and solidification processes, as well as the high cooling rates of up to 10^6 K.s^{-1} during PBF-LB [35] [36] [37] [38], these experiments only serve as a first test to assess the potential of the alloys and the copper addition regarding their magnetic properties, especially their coercivity.

The Dy content is known to have a positive impact on the coercivity of a magnet [39]. Yet, contrarily to expectations, the Alloy F with highest Dy content shows the lowest coercivity after the suction casting experiment Figure 6a. It must be mentioned that the unexpected low coercivity for Alloy F with high Dy content can be explained by its microstructure which shows a smaller fraction of RE-rich grain boundary phase than the other alloys, as depicted in the SEM-BSE images (Figure 6b,c,d). Increasing the RE content has a beneficial effect on the coercivity by forming an intergranular matrix and separating the hard magnetic $(Nd,Dy)_2Fe_{14}B$ grains. The fraction of RE rich phase in Alloy F appears to be undeniably lower in comparison to the other alloys under investigation, which explains the low coercivity despite the high Dy content. The Alloy E with a moderate Dy addition provides the highest coercivity and is used for further compositional modifications.

Starting with the selected composition, the composition was varied by increasing the Cu content by 0.4 wt.%, 0.6 wt.% and 0.8 wt.%. It is known that Cu improves the wettability of the hard magnetic phase by forming low melting eutectic with REE and, moreover, decreases the grain size in Nd-Fe-B based magnets [40] [41] [42] [43]. Pieces of the strip cast material were weighed and Cu was added systematically by arc melting the mixture 2 times, followed by another melting and suction casting. The magnetic hysteresis was then measured after the annealing cycle described in the Experimental section.

Beside the decreasing saturation magnetization, the magnetic measurements show the highest coercivity value for a Cu addition of 0.8 wt.%, as shown in Figure 7a. This measured coercivity of ~0.5 T is remarkably high for cast material and emphasizes the important effect of Cu on the magnetic properties of Nd-Fe-B magnets. The microstructure shows small grains of $(Nd,Dy)_2Fe_{14}B$ particles which are well separated by a RE rich grain boundary phase (Figure 7b). Similar to sintered Nd-Fe-B magnets, the coercivity can be explained by the fine grain size (less than 10 µm) and magnetic decoupling of the $(Nd,Dy)_2Fe_{14}B$ grains.

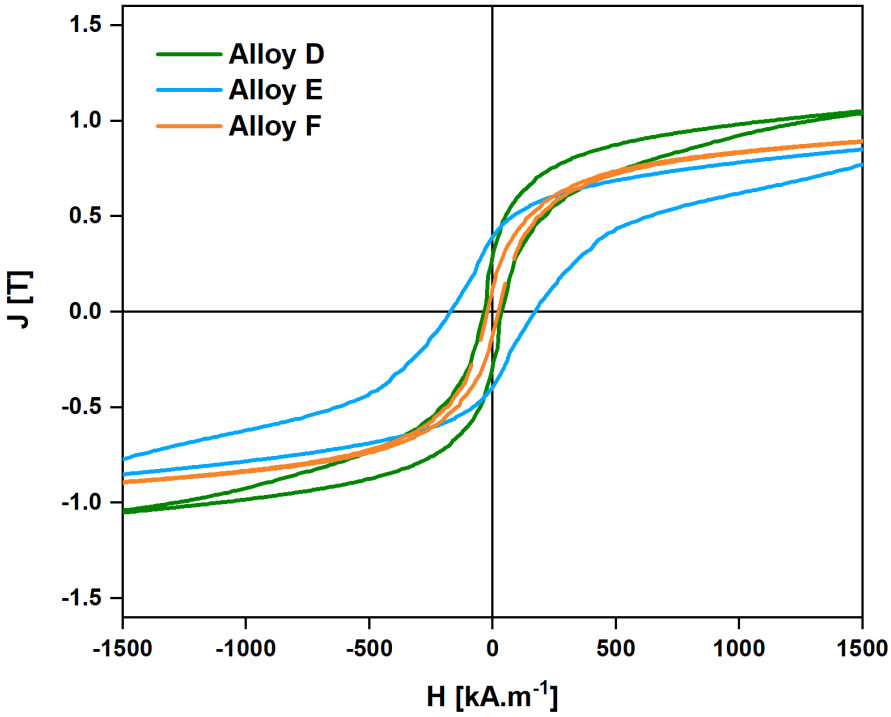

(a)

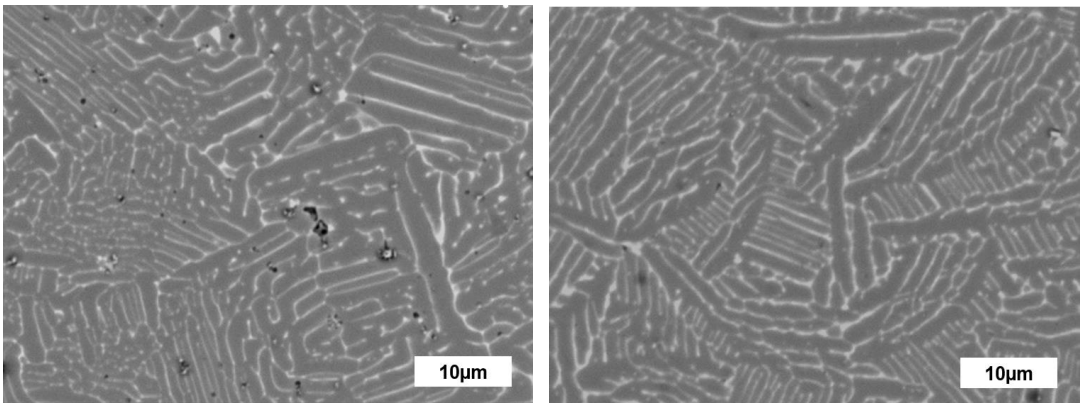

(b) (c)

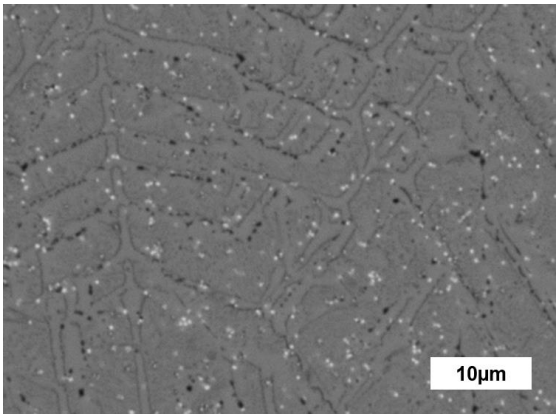

(d)

Figure 6: *(a) J-H loops of suction cast alloys of compositions D, E, F without copper addition (b, c, d) Microstructure of suction cast alloys of, respectively, composition D with no Dy, composition E with 3.7 wt.% Dy, and composition F with 10.1 wt.% Dy*

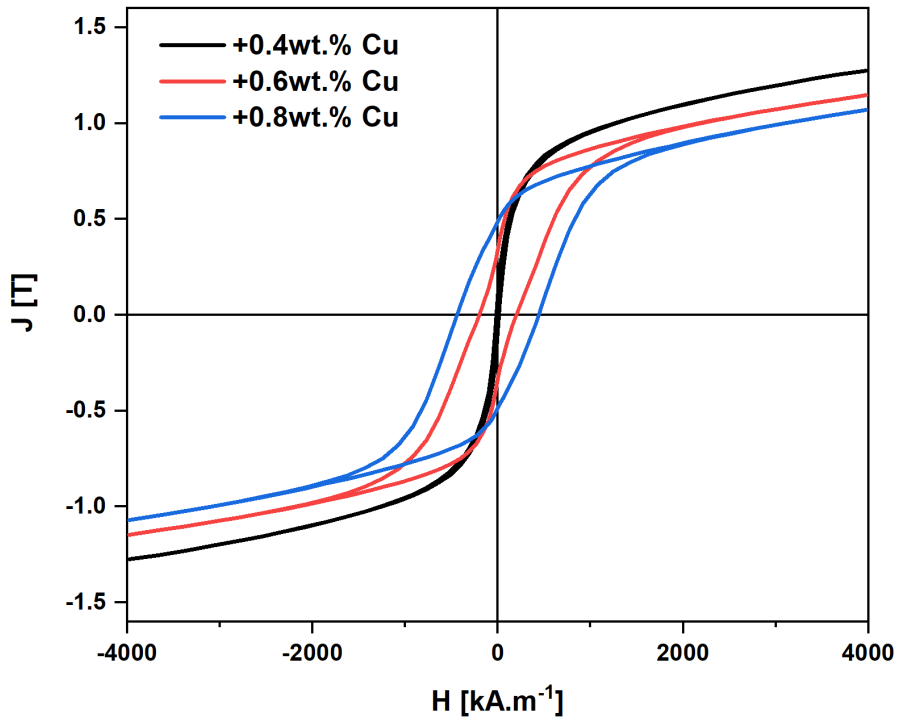

(a)

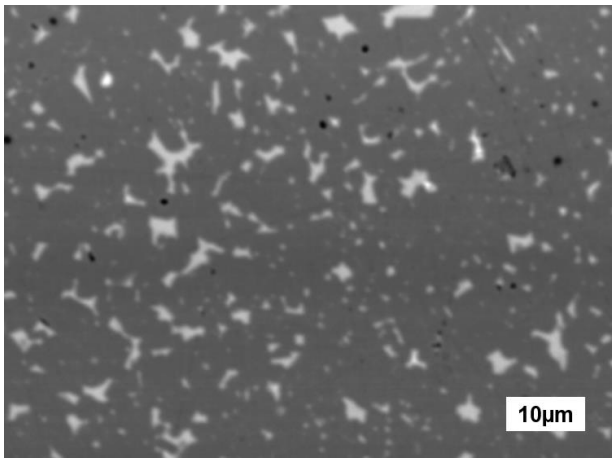

(b)

Figure 7: *(a) J-H curve of annealed suction cast samples of composition E with various copper addition rates (b) Microstructure of the suction cast alloy of composition E with 0.8 wt.% Cu addition, after annealing*

3.3 Additive manufacturing of magnets by PBF-LB

Following these preliminary experiments, additively manufactured batches were realized by PBF-LB as described before, using the Alloy E composition with an additional 0.8 wt.% Cu, yielding the aforementioned molar stoichiometry $Nd_{12.1}Pr_{0.8}Dy_{1.5}Fe_{bal.}B_{6.3}Co_{1.24}Al_1Cu_1Ga_{0.2}$. In these experiments, the layer thickness was kept constant but the laser speed, laser power and hatching distance were varied. Even though the level of cracking could be reduced after the study presented in Section 3.1, all samples present some cracks. This is reported in many publications on PBF-LB of Nd-Fe-B alloys [15] [21] [13] [24] [44] [19] and it is due to the brittle behavior of the intermetallic material [20]. The analysis of the J-H loops of the additively manufactured magnets reveals surprisingly large differences in the magnetic properties depending on the operating parameters. Figure 8a shows how the coercivity of the as-built magnets evolves with the laser speed for several values of laser speed: for speed values below a certain threshold, the coercivity is very low (< 200 $kA.m^{-1}$), whereas above the threshold, the coercivity increases dramatically to reach values as high as 1200 $kA.m^{-1}$. The threshold value increases in proportion to the laser power, which suggests that the relevant parameter may be the volumetric energy density (VED) rather that speed or laser power by itself. We define the volumetric energy density as

$$VED = \frac{P}{v.e.h}$$

where *P* stands for the laser power, *v* for the laser speed, *e* for the layer thickness and *h* for the hatching distance. The relevance and the limits of VED as a synthetic parameter has been discussed in literature [45]; in particular, VED does not capture the complexity of the physics of PBF-LB and cannot be considered as an absolute indicator. Still, within certain boundaries, it may remain an interesting hint to target a parameter window that is likely to yield good material properties. Figure 8b displays the coercivity and the relative density versus the VED for about 30 samples synthesized with moderate laser power (100 W < P < 250 W) and constant layer thickness (e = 30 µm), with varying laser power, laser speed and hatching distance. Relative density is consistently satisfying (> 94%) for VED values above 37 $J.mm^{-3}$, whereas coercivity is high (> 800 $kA.m^{-1}$) for VED values below 46 $J.mm^{-3}$, thus defining a preferential parameter window. For example, for a given laser power P, the scanning speed must be above $P/(46\ J.mm^{-3}.e.h)$ to obtain high coercivity. Figure 11 shows demagnetization curves of samples built with different VED values. It should be mentioned that samples with VED below 30 $J.mm^{-3}$ were not successfully built and do not appear in the data and that samples with coercivity above 1 T (800 $kA.m^{-1}$) all have a remanence comprised between 0.55 T and 0.60 T. Because no special means were applied to obtain grain alignment (texture), the maximum remanence value that one can expect is half of the saturation magnetization of the alloy. The alloy that was used for these experiments has a high RE content and high copper content; this decreases to the amount of Fe available to form the magnetic phase $Nd_2Fe_{14}B$, which has a saturation magnetization of 1.6 T. With this composition, only about 80 % of the volume can consist of magnetic phase, yielding a saturation magnetization of about 1.3 T. Therefore, the remanence values that were obtained with these high-coercivity samples are close to the physical limit, which is about 0.65 T for an isotropic structure. On the contrary, samples with low coercivity ($H_{cj} << B_r/\mu_0$) were measured with artificially low remanence, which is due to the self-demagnetizing of the samples between the pulsed 6 T magnetization and the close-loop J-H measurement.

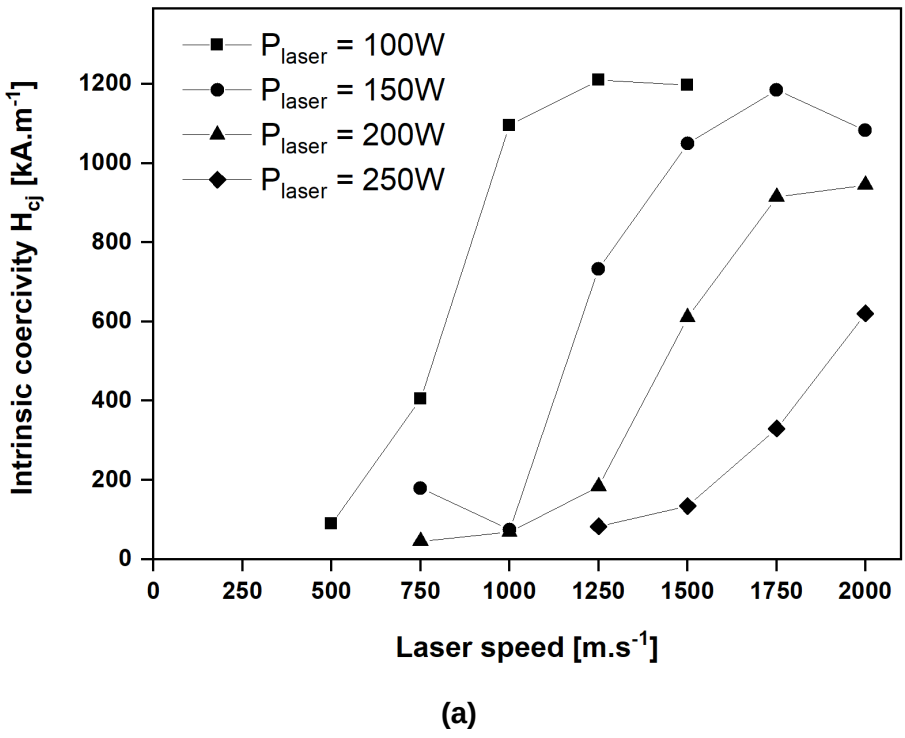

(a)

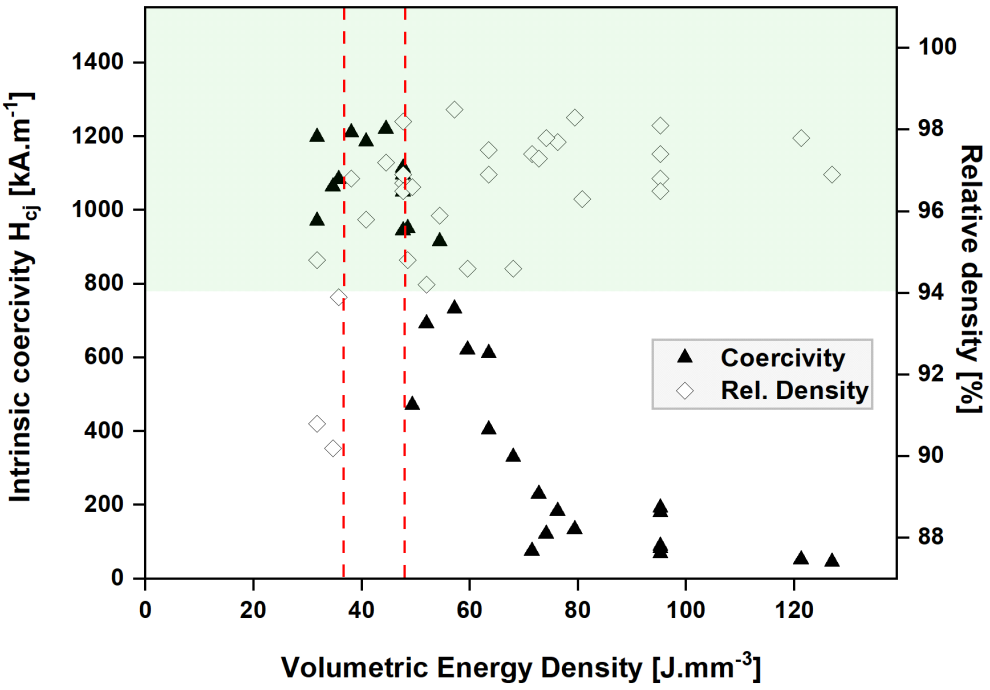

(b)

Figure 8*: (a) Coercivity of the as-built magnets as a function of laser speed for various laser power values: hatching distance is 70 µm and layer thickness 30 µm (b) Coercivity and relative density of the AM magnets as a function of VED; in this series, laser speed, laser power and hatching distance have been varied, the layer thickness is 30 µm. Red dashed lines indicate the upper and lower limit of the VED window leading to both sufficient density (>94% of theoretical) and high coercivity.*
Original data is provided in the Supplementary Material section (Table 4)

The comparative analysis of the microstructure of low-coercivity and high-coercivity samples reveals significant differences. In the samples with low coercivity (Figure 9a), α-Fe dendrites are numerous and clearly visible all over the sample, gathered along curved lines corresponding to the bottom of the melting pools. In the vicinity of these α-Fe dendrites chains, large zone with columnar magnetic phase grains can be found almost systematically. The remaining zones present an equiaxed fine-grained microstructure where the typical grain size is below 1 µm. This microstructure type is known to provide high magnetic hardness and has already been observed in PBF-LB AM magnets [13]. However, when its proportion in the magnet volume is too low, and when soft magnetic iron is ubiquitous, the magnetic hardness is lost at the macroscopic scale and the coercivity remains very low. On the contrary, samples that have a high coercivity in the as-built state contain almost no α-Fe dendrites and most of the volume is occupied by equiaxed fine grains (Figure 9b). These differences in the microstructure are due to the cooling rate corresponding to different VED values: if the VED is just sufficient to melt the last powder layer with only shallow re-melting of previous layers, the quenching of the alloy after the laser melting is very fast, which favors the emergence of a submicronic equiaxed microstructure (Figure 9c) and impedes the formation of α-Fe and the dendritic growth of the 2:14:1 phase, as shown in previous works [13] [15]. On the contrary, if the VED is higher, the laser provides excess energy that causes a bigger melt pool and deeper re-melting, and therefore a reduction of the thermal gradient and cooling rate, thus enabling the columnar growth of the 2:14:1 phase and giving sufficient time for iron dendrites to form and dendrites to grow. These trends can be to some extent influenced by compositional changes of the alloy, and this work shows that a 0.8wt.% copper addition (i.e. about 5-8 times more copper than in standard sintered Nd-Fe-B compositions) is helpful to promote the small-grained equiaxed microstructure. The oxygen content of the additively manufactured samples is about 1400 ppm, whereas the oxygen content of the as-cast ribbons is about 200 ppm. This moderate oxygen uptake, comparable to the sintering process, could be achieved thanks to the low amount of fine particles in the powder combined to the good tightness of the PBF-LB equipment and transfer vessels.

Annealing of the AM magnets was carried out after preliminary differential scanning calorimetry experiments, which allowed to estimate that a liquid phase appears at about 440°C for this composition (Figure 10). The best annealing condition generally comprises a last plateau at a temperature slightly above the temperature of apparition of the first liquid phase of the alloy. The annealing study was focused on samples that already had a high coercivity in the as-built state. Figure 11 shows demagnetization curves of as-built and annealed samples. Remanence does not exceed 0.65 T, which is the maximum value expected for Nd-Fe-B alloys without grain alignment. The absence of texture was confirmed by magnetic measurements done on other samples which had a cubic shape, and which we measured along the three axes, obtaining exactly the same J(H) curves in the three directions. In parallel, some attempts to obtain texture with laser patterns without rotation of the scanning direction between successive layers were carried out unsuccessfully, i.e. the remanence remained below 0.65 T.

The plateau temperature providing the larger coercivity enhancement appeared to be between 470°C and 490°C, with a coercivity as high as 1765 $kA.m^{-1}$. However, this condition does not allow to remove the few α-Fe dendrites present in the as-built state, and no obvious modification of the microstructure can be pointed out with standard SEM microscopy. The dissolution of α-Fe dendrites can be achieved with an annealing plateau at 600°C, but its duration has to remain very short in order to avoid grain growth. For this reason, a 10-min plateau at 600°C followed by a second plateau at lower temperature has proved to produce good results [13] and was applied in this work. Eventually, the better magnetic properties were obtained with a 2-stage annealing, with a first 10-min plateau at 600°C followed by a 1-hour plateau at 470°C, with a cooling speed equal to $30°C.min^{-1}$ after each plateau. Figure 9d displays the microstructure of this sample with the optimal annealing cycle, showing the complete removal of α-Fe dendrites and the absence of noticeable grain growth.

Table 2 summarizes the best magnetic properties of the PBF-LB processed magnets in this work.

Best magnetic properties of PBF-LB processed magnets with 0.96wt.% Cu content built with 38<VED<46 J.mm^{-3}	**B_r [T]**	**H_{cj} [kA.m^{-1}]**	**BH_{max} [kJ.m^{-3}]**
As-built	0.58	1210	48.2
After 1h-470°C annealing	0.61	1761	60.0
After 10min-600°C + 1h-470°C annealing	0.62	1790	65.0

Table 2*: Magnetic properties achieved in PBF-LB 0.96wt.% Cu PBF-LB processed magnets with 38 < VED < 46 J.mm^{-3}*

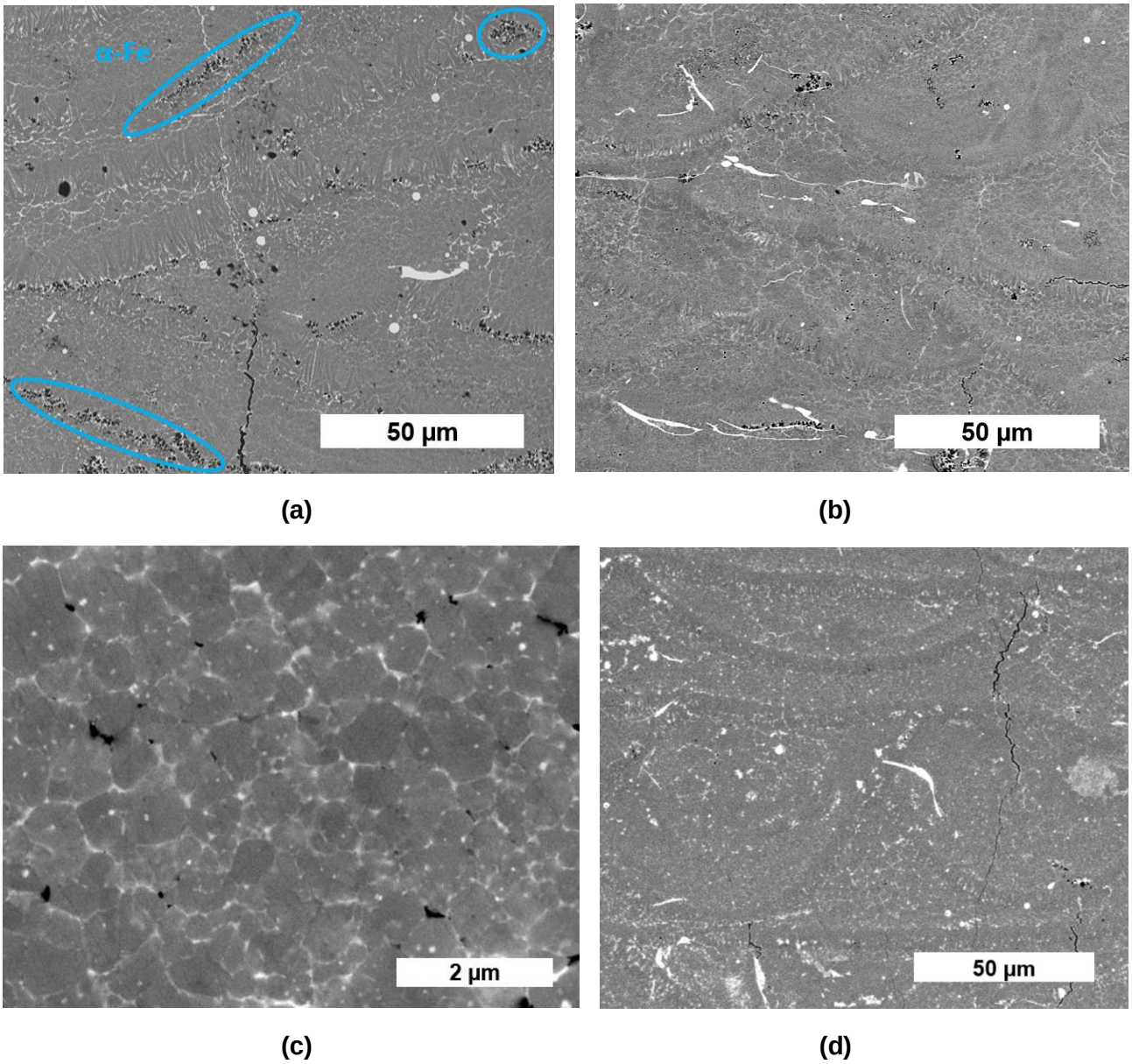

Figure 9*: Microstructures of dense (95%) PBF-LB processed magnets (a) with high energy density and low coercivity; some zones containing numerous α-Fe dendrites are marked by blue circles (b) with low energy density and high coercivity (c) same sample as (b) with higher magnification (d) with low energy density and high coercivity, after a two-step 600°C + 470°C thermal annealing*

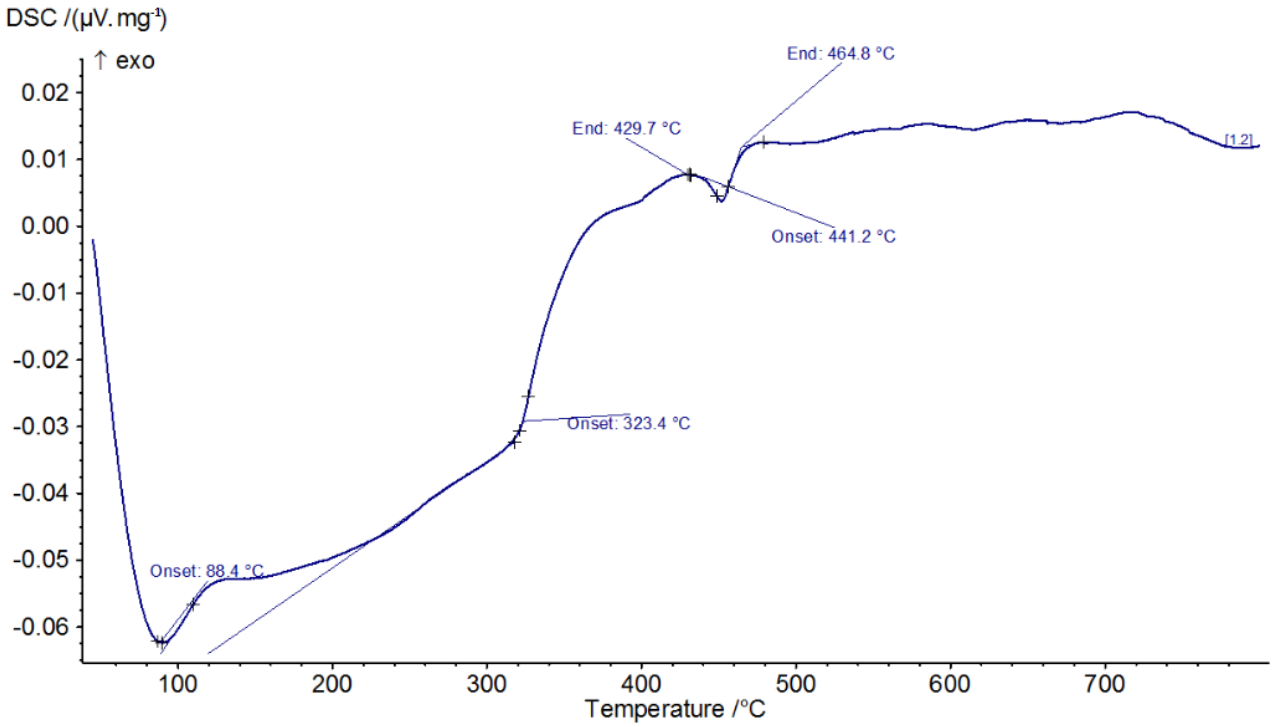

Figure 10: *Differential Scanning Calorimetry curve of a PBF-LB processed Nd-Fe-B sample with copper-rich composition, revealing the apparition of liquid phase at temperatures at 441°C (lower than standard Nd-Fe-B alloy).*

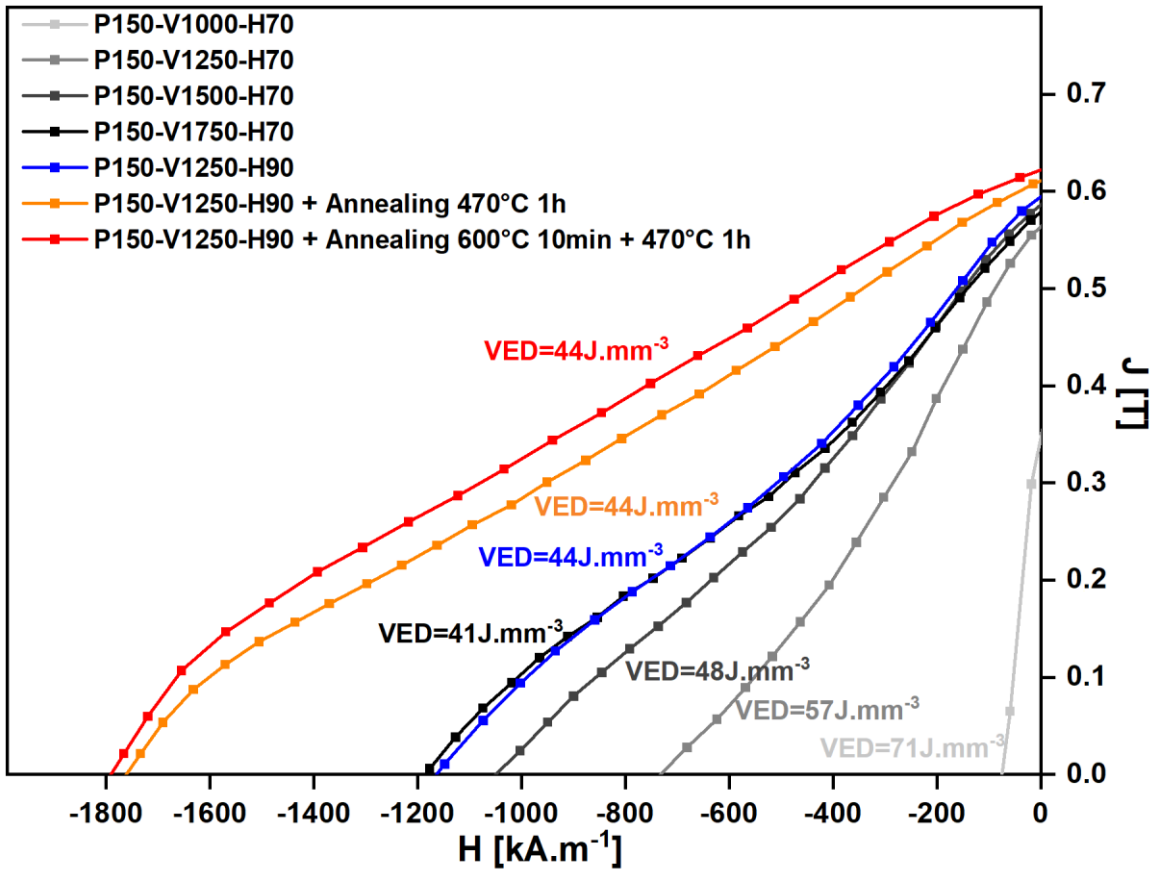

Figure 11*: Demagnetization curves of PBF-LB processed magnets with various volumetric energy densities (in grey), and with thermal annealing or not (in color). In the legend, **Pxxx** stands for the laser power in W, **Vxxx** stands for the laser velocity in mm.s-1, and **Hxx** stands for the hatching distance in microns.*

4. Conclusion

In this study, we have presented a method for screening the alloy composition of Nd-Fe-B magnets for PBF-LB using single track scanning and suction casting, to ultimately produce magnets using PBF-LB from non-spherical jet milled powder. Using this approach, a copper-rich Nd-Fe-B composition was synthesized by a process close to the industrial standards (strip casting, annealing, hydrogen decrepitation, nitrogen jet milling), and high coercivity isotropic Nd-Fe-B magnets realized from this powder using PBF-LB. Magnetic properties (after annealing) of B_r = 0.62 T, H_{cj} = 1790 kA.m^{-1} and BH_{max} = 65 kJ.m^{-3} were obtained, showing the possibility to produce magnets with PBF-LB having high coercivity comparable to sintered magnets. This represents the highest reported coercivity for additively manufactured Nd-Fe-B magnets as of today (

Figure 12). A relatively low energy input (VED = 38–46 J.mm^{-3} in this study) during PBF-LB processing was identified necessary to realize high coercivity, as low energy input leads to a small melt pool size, extremely rapid cooling and hence a fine, equiaxed microstructure without dendrite growth or excessive α-Fe is formed. Further studies should focus on inducing grain alignment to PBF-LB processed Nd-Fe-B magnets to reach higher remanence and energy product.

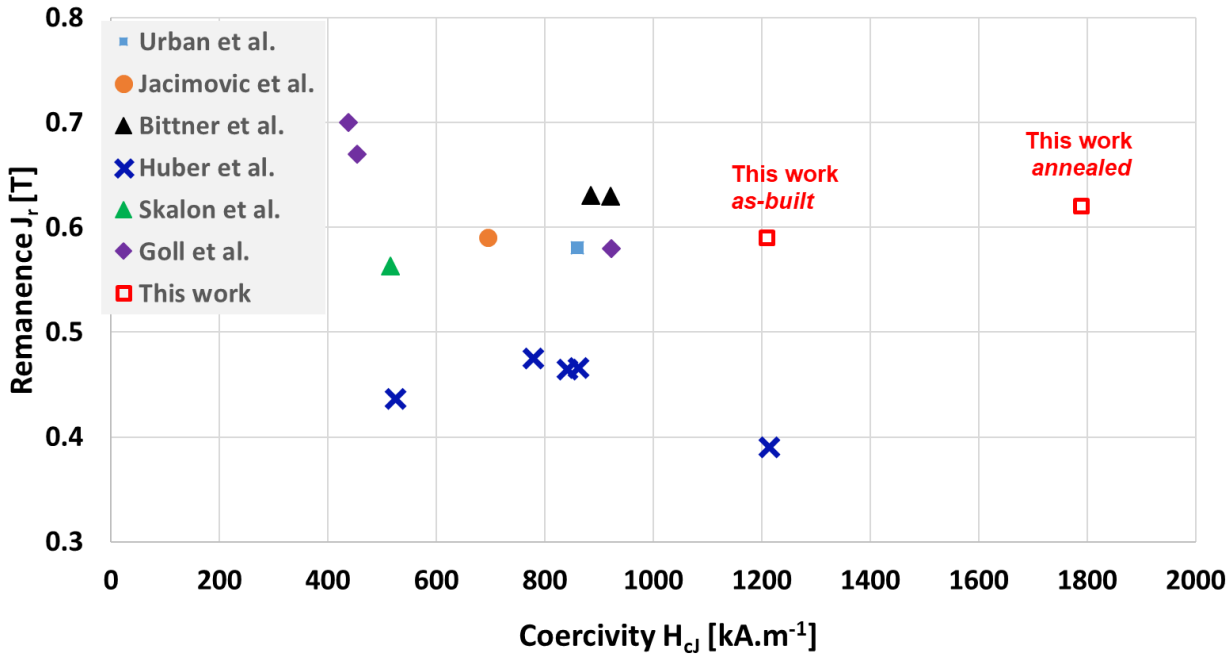

Figure 12: *Results of this work compared to state-of-the-art Nd-Fe-B magnets synthetized by PBF-LB* [15] [17] [18] [19] [20] [21] [13] [24]

CRediT authorship contribution statement

Olivier Tosoni: Conceptualization, Methodology, Investigation, Writing.

Elisa Borges: Methodology, Data curation, Investigation

Joni Reijonen: Conceptualization, Methodology, Investigation, Writing, Project administration

Atte Antikainen: Conceptualization, Methodology, Investigation, Writing

Lukas Schäfer: Conceptualization, Methodology, Investigation, Writing

Stefan Riegg: Conceptualization, Methodology

Oliver Gutfleisch: Conceptualization, Writing, Supervision, Validation

Declaration of Competing Interest

The authors declare that they have no known competing financial interests or personal relationships that could have appeared to influence the work reported in this paper.

Acknowledgment

The authors would like to express special gratitude to Mr. Bastien Marchais (CEA) for this help in the PBF-LB experiments and to Jürgen Gassmann from the Fraunhofer IWKS Institute Hanau for supplying the Nd-Fe-B alloys. TUDa also thanks the DFG Collaborative Research Centre/Transregio 270 HoMMage Project ID No. 405553726, TRR 270 (projects A01, A10). This work was conducted under the EIT Raw Materials funded 3DREMAG project (project number 19242).

References

[1] R. Gauss, B. C., F. Carencotte, M. Gasparon, O. Gutfleisch, I. Higgins, M. Karajić, A. Klossek, M. Mäkinen, B. Schäfer, R. Schindler and V. B., "Rare Earth Magnets and Motors: A European Call for Action. A report by the Rare Earth Magnets and Motors Cluster of the European Raw Materials Alliance," Berlin, 2021.

[2] O. Gutfleisch, M. Willard, E. Brück, C. Chen, S. Sankar and J. Liu, "Magnetic Materials and Devices for the 21st Century: Stronger, Lighter, and More Energy Efficient," *Advanced Materials,* vol. 23, p. 821–842, 2011.

[3] Y. Matsuura, "Recent development of Nd–Fe–B sintered magnets and their applications," *Journal of Magnetism and Magnetic Materials,* vol. 303, no. 2, pp. 344-347, 2006.

[4] C. Huber, C. Abert, F. Bruckner, M. Groenefeld, S. Schuschnigg, I. Teliban, C. Vogler, G. Wautischer, R. Windl and D. Suess, "3D Printing of Polymer-Bonded Rare-Earth Magnets With a Variable Magnetic Compound Fraction for a Predefined Stray Field," *Scientific Reports,* vol. 7, p. 9419, 2017.

[5] B. A.B., P. P., W. P.A.P., A. C.H. and J. Mascheroni, "Additive Manufacturing of Bonded Nd-Fe-B - Effect of Process Parameters on Magnetic Properties," *IEEE Transactions on Magnetics,* vol. 53, no. 11, p. 7948722, 2017.

[6] B. Compton, J. Kemp, T. Novikov, R. Pack, C. Nlebedim, C. Duty, O. Rios and M. P. Paranthaman, "Direct-write 3D printing of NdFeB bonded magnets," *Materials and Manufacturing Processes,* vol. 33, no. 1, pp. 109-113, 2018.

[7] K. Gandha, I. Nlebedim, V. Kunc, E. Lara-Curzio, R. Fredette and M. Paranthaman, "Additive manufacturing of highly dense anisotropic Nd–Fe–B bonded magnets," *Scripta Materialia,* vol. 183, pp. 91-95, 2020.

[8] A. Sarkar, M. Paranthaman and I. Nlebedim, "In-situ magnetic alignment model for additive manufacturing of anisotropic bonded magnets," *Additive Manufacturing,* vol. 46, p. 102096, 2021.

[9] H. Mitarai, K. Noguchi, C. Mishima, H. Matsuoka, M. Yamazaki and Y. Kawasugi, "Development of Compound for Anisotropic Bonded Nd Magnets Using d-HDDR Magnet Powder," *IEEE Transactions on Magnetics,* vol. 50, no. 11, pp. 1-3, 2014.

[10] Y. Zhang, L. Wu, X. Guo, S. Kane, Y. Deng, Y.-G. Jung, J.-H. Lee and J. Zhang, "Additive Manufacturing of Metallic Materials: A Review," *Journal of Materials Engineering and Performance,* vol. 27, pp. 1-13, 2018.

[11] S. Gruber, C. Grunert, M. Riede, E. López, A. Marquardt, F. Brueckner and C. Leyens, "Comparison of dimensional accuracy and tolerances of powder bed based and nozzle based additive manufacturing processes," *Journal of Laser Applications,* vol. 32, p. 032016, 2020.

[12] L. Liu, Q. Ding, Y. Zhong, J. Zou, J. Wu, Y.-L. Chiu, J. Li, Z. Zhang, Q. Yu and Z. Shen, "Dislocation network in additive manufactured steel breaks strength–ductility trade-off," *Materials Today,* vol. 21, no. 4, pp. 354-361, 2018.

[13] D. Goll, F. Trauter, T. Bernthaler, J. Schanz, H. Riegel and G. Schneider, "Additive Manufacturing of Bulk Nanocrystalline FeNdB Based," *Micromachines,* vol. 12, p. 538, 2021.

[14] J. D. Moore, D. Klemm, D. Lindackers, S. Grasemann, R. Träger, J. Eckert, L. Löber, S. Scudino, M. Katter, A. Barcza, K. P. Skokov and O. Gutfleisch, "Selective laser melting of La(Fe,Co,Si)13 geometries for magnetic refrigeration," *J. Appl. Phys.,* vol. 114, no. 043907 1-8, 2013.

[15] J. Jaćimović, F. Binda, L. Herrmann, F. Greuter, J. Genta, M. Calvo, T. Tomše and R. Simon, "Net Shape 3D Printed NdFeB Permanent Magnet," *Advanced Engineering Materials,* vol. 19, no. 8, p. 1700098, 2017.

[16] N. Urban, F. Huber and J. Franke, "Influences of process parameters on Rare Earth Magnets produced by Laser Beam Melting," in *7th International Electric Drives Production Conference, EDPC 2017*, Würzburg, 2017.

[17] N. Urban, A. Meyer, V. Keller and J. Franke, "Contribution of Additive Manufacturing of Rare Earth Material to the Increase in Performance and Resource Efficiency of Permanent Magnets," *Applied Mechanics and Materials,* vol. 882, pp. 135-141, 2018.

[18] M. Skalon, M. Görtler, B. Meier, S. Arneitz, N. Urban, S. Mitsche, C. Huber, J. Franke and C. Sommitsch, "Influence of Melt-Pool Stability in 3D Printing of NdFeB Magnets on Density and Magnetic Properties," *2020,* vol. 13, p. 139, 2020.

[19] F. Bittner, J. Thielsch and W. Drossel, "Microstructure and magnetic properties of Nd-Fe-B permanent magnets produced by laser powder bed fusion," *Scripta Materialia,* p. 113921, 2021.

[20] F. Bittner, J. Thielsch and W. Drossel, "Laser powder bed fusion of Nd–Fe–B permanent magnets," *Progress in Additive Manufacturing,* vol. 5, pp. 3-9, 2020.

[21] C. Huber, H. Sepehri-Amin, M. Goertler, M. Groenefeld, I. Teliban, K. Hono and D. Suess, "Coercivity enhancement of selective laser sintered NdFeB magnets by grain boundary infiltration," *Acta Materialia,* vol. 172, pp. 66-71, 2019.

[22] A. Volegov, S. Andreev, N. Selezneva, I. Ryzhikhin, N. Kudrevatykh, L. Mädler and I. Okulov, "Additive manufacturing of heavy rare earth free high-coercivity permanent magnets," *Acta Materialia,* vol. 188, pp. 733-739, 2020.

[23] L. Schäfer, K. Skokov, J. Liu, F. Maccari, T. Braun, S. Riegg, I. Radulov, J. Gassmann, M. Merschroth, J. Harbig, M. Weigold and O. Gutfleisch, "Qualification of Pr-Fe-Cu-B Alloys for the Additive Manufacturing of Permanent Magnets by alloy design," *Advanced Functional Materials,* p. 2102148, 2021.

[24] D. Goll, F. Trauter, R. Loeffler, T. Gross and G. Schneider, "Additive Manufacturing of Textured FePrCuB," *Micromachines,* vol. 12, p. 1056, 2021.

[25] I. Yadroitsev, A. Gusarov, I. Yadroitsava and I. Smurov, "Single track formation in selective laser melting of metal powders," *J. Mater. Process. Technol.,* vol. 210, pp. 1624-1631, 2010.

[26] S. Ghosh, L. Ma, L. Levine, R. Ricker, M. Stoudt, J. Heigel and J. Guyer, "SingleTrack Melt-Pool Measurements and Microstructures in Inconel 625," *JOM,* vol. 70, pp. 1011-1016, 2018.

[27] N. Aboulkhair, I. Maskery, C. Tuck, I. Ashcroft and N. Everitt, "On the formation of AlSi10Mg single tracks and layers in selective laser melting: Microstructure and nano-mechanical properties," *J. Mater. Process. Technol.,* vol. 230, pp. 88-98, 2016.

[28] A. Aversa, M. Moshiri, E. Librera, M. Hadi, G. Marchese, D. Manfredi, M. Lorusso, F. Calignano, S. Biamino, M. Lombardi and M. Pavese, "Single scan track analyses on aluminium based powders," *J. Mater. Process. Technol.,* vol. 255, pp. 17-25, 2018.

[29] M. L. H. H. Z. Fan, "Selective laser melting of alumina: A single track study," *Ceram. Int.,* vol. 44, pp. 9484-9493, 2018.

[30] T. Kozieł, "Estimation Of Cooling Rates In Suction Casting And Copper-Mould Casting Processes," *Arch. Metall. Mater.,* vol. 60, no. 2, pp. 767-771, 2015.

[31] R. M. Srivastava, J. Eckert, W. Löser, B. Dhindaw and L. Schultz, "Cooling rate evaluation for bulk amorphous alloys from eutectic microstructures in casting processes," *Mater. Trans.,* vol. 43, no. 7, pp. 1670-1675, 2002.

[32] P. Pawlik, K. Pawlik and A. Przybył, "Investigation of the cooling rate in the suction casting process," *Rev. Adv. Mater. Sci.,* vol. 18, no. 1, pp. 81-84, 2008.

[33] A. Antikainen, J. Reijonen, J. Lagerbom, M. Lindroos, T. Pinomaa and T. Lindroos, "Single-Track Laser Scanning as a Method for Evaluating Printability: The Effect of Substrate Heat Treatment on Melt Pool Geometry and Cracking in Medium Carbon Tool Steel," *Journal of Materials Engineering and Performance,* 2022.

[34] W. Jhang Jian, C. Cheng, W. Chang, T. Huang, Y. L. A. Liang, T. Chang and M. Tsai, "Fabrication of crack-free Nd-Fe-B magnets with laser powder bed fusion," *Materialia,* vol. 21, p. 101351, 2022.

[35] A. Hooper, "Melt pool temperature and cooling rates in laser powder bed fusion," *Additive Manufacturing,* vol. 22, pp. 548-559, 2018.

[36] T. Vilaro, C. Colin and J. Bartout, "As-fabricated and heat-treated microstructures of the Ti-6Al-4V alloy processed by selective laser melting," *Metallurgical and Materials Transactions A: Physical Metallurgy and Materials Science,* vol. 42, no. 10, pp. 3190-3199, 2011.

[37] R. H. m. t. R. H.K., R. H.K., K. N.V., H. Gong, T. Starr and B. Stucker, "Microstructures and mechanical properties of Ti6Al4V parts fabricated by selective laser melting and electron beam melting," *Journal of Materials Engineering and Performance,* vol. 22, no. 12, pp. 3872-3883, 2013.

[38] D. Buchbinder, H. Schleifenbaum, S. Heidrich, W. Meiners and B. J. , "High Power Selective Laser Melting (HP SLM) of Aluminum Parts," *Physics Procedia,* vol. 12, pp. 271-278, 2011.

[39] M. Sagawa, S. Hirosawa, H. Yamamoto, S. Fujimura and Y. Matsuura, "Nd-Fe-B permanent magnet materials," *Jpn. J. Appl. Phys.,* vol. 26, p. 785, 1987.

[40] J. J. Fidler and T. Schrefl, "Overview of Nd–Fe–B magnets and coercivity," *J. Appl. Phys., vol.,* vol. 79, no. 8, p. 5029, 1996.

[41] X. Xu, H. Sepehri-Amin, T. Sasaki, M. Soderžnik, X. Tang, T. Ohkubo and K. Hono, "Comparison of coercivity and squareness in hot-deformed and sintered magnets produced from a Nd-Fe-B-Cu-Ga alloy," *Scr. Mater.,,* vol. 160, pp. 9-14, 2019.

[42] S. Pandian, V. Chandrasekaran, G. Markandeyulu, K. J. L. Iyer and K. V. S. Rama Rao, "Effect of Al, Cu, Ga, Nb additions on the magnetic properties and microstructural features of sintered NdFeB," *J. Appl. Phys.,* vol. 92, no. 10, pp. 6082-6086.

[43] W. Li, T. T. Ohkubo, T. Akiya, H. Kato and K. Hono, "The role of Cu addition in the coercivity enhancement of sintered Nd-Fe-B permanent magnets," *J. Mater. Res.,* vol. 24, no. 2, pp. 413-420, 2009.

[44] M. Emminghaus, C. Hoff, J. Hermsdorf and S. Kaierle, "Laser Powder Bed Fusion of NdFeB and influence of heat treatment on microstructure and crack development," *Procedia CIRP 94,* pp. 211-216, 2020.

[45] U. Bertoli, A. Wolfer and M. Matthews, "On the limitations of Volumetric Energy Density as a design parameter," *Materials and Design,* vol. 113, pp. 331-340, 2017.

[46] M. Skalon, M. Görtler, B. Meier, S. Arneitz, N. Urban, S. Mitsche, C. Huber, J. Franke and C. Sommitsch, "Influence of melt-pool stability in 3D printing of NdFeB magnets on density and magnetic properties," *Materials,* vol. 13, no. 1, p. 139, 2020.

Supplementary material

		Width of the laser track [µm]					
Scanning speed [mm.s^{-1}]	**Laser power [W]**	**Alloy A**	**Alloy B**	**Alloy C**	**Alloy D**	**Alloy E**	**Alloy F**
800	150	154	142	151	174	174	183
1000	200	134	133	165	146	172	191
1300	160	124	130	117	120	134	129
1250	75	75	82	86	119	103	92
1500	100	91	91	95	97	109	98
1750	125	100	98	104		122	103
2000	150	103	111	104	111	126	109
800	70	101	98	103	102	126	105
2000	200	117	123	122	126	136	125
500	50	107	106	109	107	128	117
1500	150	114	110	114	118	133	118
1000	100	107	104	107	114	142	110
1750	175	113	111	117	124	124	116
1250	125	107	108	109	113	126	103
1500	200	119	118	120	125	146	124
1054	158	118	120	125	132	171	146
777	116,5	147	146	159	150	186	154
500	75	154	149	159	160		152
1250	200	120	126	120	122		137

(a)

		Penetration depth [µm]					
Scanning speed [mm.s^{-1}]	**Laser power [W]**	**Alloy A**	**Alloy B**	**Alloy C**	**Alloy D**	**Alloy E**	**Alloy F**
800	150	130	110	142	147	134	135
1000	200	133	133	147	149	165	152
1300	160	80	80	88	90	102	90
1250	75	34	39	40	44	52	45
1500	100	40	50	46	50	62	53
1750	125	57	45	53		61	55
2000	150	46	46	52	55	65	59
800	70	56	54	55	59	68	63
2000	200	68	75	69	75	85	74
500	50	57	56	56	60	76	64
1500	150	71	63	72	79	92	75
1000	100	64	64	67	67	81	68
1750	175	69	66	72	75	88	76
1250	125	67	69	74	71	86	69
1500	200	90	88	101	91	119	109
1054	158	93	98	110	103	131	101
777	116,5	92	100	100	93	118	109
500	75	96	96	101	103	153	105
1250	200	101	111	118	107		112

(b)

Table 3*: Data relative to the* Figure *5 (a) Width of the laser tracks and (b) penetration depth of the melting in single scan melting experiments*

Scanning speed V [mm.s^{-1}]	Laser power P [W]	Hatching distance H [µm]	Volumetric Energy Density VED [J.mm^{-3}]	Intrinsic coercivity H_{cj} [kA.m^{-1}]	Remanence B_r [T]	Energy product BH_{max} [J.mm^{-3}]	Relative density [%]
250	50	70	95	193	0.45	16.9	97.4
500	50	70	48	1115	0.59	48.9	96.7
500	100	70	95	89	0.36	7.2	98.1
750	100	70	63	404	0.51	26.1	97.5
750	100	90	49	470	0.56	24.1	96.9
1250	100	55	48	951	0.48	31.3	96.8
1000	100	70	48	1096	0.58	46.9	94.8
1250	100	70	38	1210	0.58	46.2	96.8
1750	100	55	35	1063	0.54	36.7	97.4
1500	100	70	32	1197	0.58	46.1	98.5
750	150	55	121	51	0.25	3.1	98.2
750	150	70	95	179	0.44	15.3	95.8
1250	150	55	73	229	0.47	17.7	93.9
750	150	90	74	121	0.42	6.7	96.9
1000	150	70	71	75	0.35	5.0	97.4
1250	150	70	57	733	0.56	38.4	97.7
1750	150	55	52	692	0.54	34.6	96.9
1500	150	70	48	1050	0.59	46.6	95.9
1250	150	90	44	1219	0.57	45.6	96.5
1750	150	70	41	1185	0.58	46.0	96.5
2000	150	70	36	1083	0.53	37.3	98.3
1750	150	90	32	970	0.52	30.2	94.6
750	200	70	127	45	0.19	2.1	94.6
1000	200	70	95	69	0.31	4.3	90.8
1250	200	70	76	183	0.44	14.0	90.2
1500	200	70	63	611	0.54	31.5	97.2
1750	200	70	54	915	0.55	36.5	94.8
2000	200	70	48	945	0.57	43.0	96.6
1250	250	70	95	83	0.31	4.0	94.2
1500	250	70	79	134	0.40	10.7	97.3
1750	250	70	68	330	0.49	19.6	97.8
2000	250	70	60	620	0.52	28.5	96.3

Table 4*: Data relative to the Figure 8 – Intrinsic coercivity, remanence, energy product and relative density as a function of process parameters*